DE GRUYTER Nanotechnology Reviews 2021; 10: 807–818

Research Article

Zheyu Zhu, Zhongping Wang, Yue Zhou, Yuting Chen, Long Zhou, and Anming She*

Evaluation of the nanostructure of calcium silicate hydrate based on atomic force microscopy-infrared spectroscopy experiments

https://doi.org/10.1515/ntrev-2021-0059
received July 2, 2021; accepted August 1, 2021

Abstract: Calcium silicate hydrate (C–S–H) is the main product of cement hydration, which forms the microstructure of cement *via* the stacking of basic nanocrystals or gel units, and has a substantial influence on the mechanical performance of cement. Tetrahedron chains of silicon oxide form the main nanoscale structure of basic C–S–H units. Evaluation on the nanostructure of these tetrahedron chains facilitates to understand the source of cement strength. This article first introduced the atomic force microscopy-infrared spectroscopy (AFM-IR) technique into evaluating the nanostructure of C–S–H. The nano infrared spectroscopy of stacking C–S–H nanograins and tetrahedron spatial distribution mapping was obtained. The results demonstrate that the relative quantity of tobermorite-like and jennite-like units in C–S–H nanograins can be analyzed by AFM-IR. The stacking between C–S–H particles is facilitated to a large extent by silicate (SiO_4^{2-}) tetrahedron chains formed of three tetrahedrons bridged by two oxygen atoms (*i.e.*, Q^2 chains), and there are Q^2 chains acting as bridges between C–S–H particles. The proportions of different types of Q^2 chains available for facilitating C–S–H particle stacking vary at the nanoscale. AFM-IR spatial mapping demonstrate that the orientations of these Q^2 chains are not evenly distributed. These findings provide experimental information of the stacking C–S–H gaps.

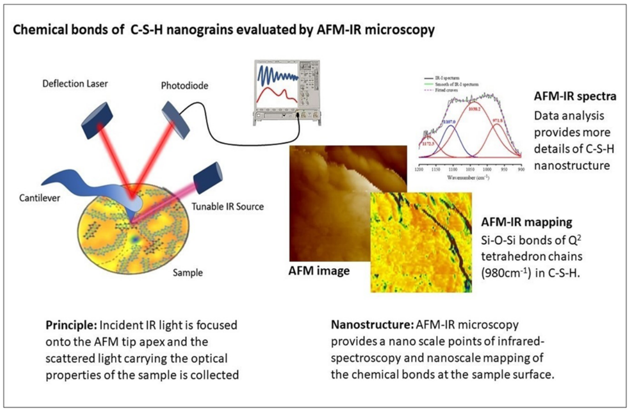
Chemical bonds of C-S-H nanograins evaluated by AFM-IR microscopy

Principle: Incident IR light is focused onto the AFM tip apex and the scattered light carrying the optical properties of the sample is collected

Nanostructure: AFM-IR microscopy provides a nano scale points of infrared-spectroscopy and nanoscale mapping of the chemical bonds at the sample surface.

Graphical abstract

Keywords: cement, calcium silicate hydrate, AFM-IR, Q^2 tetrahedron chain, deconvolution

1 Introduction

Cement is a widely used bionic material (*i.e.*, artificial bone) and building material with a long history. The modification of cement by additives can enhance the performance. The common successful modifications are preparing cement composites by addition of polymers, fibers, nanoparticles *etc*. Rostami *et al.* [1] designed the composites of superabsorbent polymers, polypropylene fiber, and mortars, which successfully reduce shrinkage. Since the source of cement strength is related to the microstructure of hydrates, it is noteworthy that the composites mentioned above can be enhanced based on a deeper understanding of calcium silicate hydrate (C–S–H) nanostructure, especially nano-chemical bonds of C–S–H aggregates.

The main product of cement hydration is C–S–H, which represents 60–70% of the final product by weight [2]. And C–S–H has a substantial influence on the mechanical performance of cement-based materials [3]. Papatzani *et al.* [4] summarized the review of the models on the

---

*** Corresponding author: Anming She,** School of Materials Science and Engineering, Tongji University, Shanghai 201804, China; Key Laboratory of Advanced Civil Engineering Materials of Ministry of Education, Tongji University, Shanghai 201804, China, e-mail: sheanming@tongji.edu.cn
Zheyu Zhu, Yue Zhou, Yuting Chen, Long Zhou: School of Materials Science and Engineering, Tongji University, Shanghai 201804, China
Zhongping Wang: School of Materials Science and Engineering, Tongji University, Shanghai 201804, China; Key Laboratory of Advanced Civil Engineering Materials of Ministry of Education, Tongji University, Shanghai 201804, China

nanostructure of calcium silicate hydrates and described that the basic C–S–H unit has a complex nanoscale structure formed of silicate (SiO_4^{2-}) tetrahedron chains, and a very large specific surface area. This SiO_4^{2-} chain structure of C–S–H units is what provides cement-based materials with the necessary mechanical strength for use as building materials, but is also useful for the development of other materials, such as biological materials, mortars, and drugs.

Although the nanostructure of C–S–H has been studied for more than one century, there are still debates about the actual structure of C–S–H. The microstructure of C–S–H is currently subject to a debate between crystalline and gel models. Zhu *et al.* [5] summarized the review of crystalline models indicating crystalline C–S–H structure similar to natural minerals. In contrast, the gel models consider C–S–H as the progressive accumulation of nanoscale C–S–H particles to form larger-scale amorphous C–S–H colloids that are further accumulated to form the final gel structure. The review of gel models was also summarized by Zhu *et al.* [6]. A comparison of these approaches indicates that crystalline models focus more on the nanostructure of the basic C–S–H unit, while gel models focus more on the way in which basic C–S–H units stack with each other. These two perspectives can separately explain aspects of the observed experimental phenomena, but neither can explain a number of the features of C–S–H independently. Jennings considered both crystalline and gel properties to refine the colloidal model of C–S–H by proposing the widely accepted CM-II model, which treats C–S–H as a stacking of nanoscale crystalline units (commonly within 10 nm) [7]. Based on the recent C–S–H model, Hou *et al.* [8] investigated the structure, mechanical properties, and the crack propagation of the colloidal C–S–H gel at the mesoscale by molecular dynamics simulation, and demonstrated that both the strength and Young's modulus grow exponentially with the increase in the packing fraction which shows reasonable agreement with the literature. Despite this, CM-II model still needs more details. The difficulties are to obtain the real ratios of different crystal units at nanoscale as well as the lacking experimental information of chemical bonds between C–S–H stacking particles.

Bulk C–S–H is a layered-like material at nanoscale. Accordingly, efforts to understand the structure of C–S–H have also benefited from comparisons with the structures of naturally occurring layered minerals. Polisi *et al.* [9] described that tobermorite and jennite conform to the $CaO–SiO_2–H_2O$ system. Huang *et al.* [10] described the nanoscale structure of C–S–H in terms of layered tobermorite-like or jennite-like structures. Zhou and Liang [11] built C–S–H models by molecular dynamics simulation and pointed out that C–S–H includes defects in its SiO_4^{2-} chains. The structure of each layer in tobermorite is formed of SiO_4^{2-} chains that are distributed in parallel, and the middle points of the chains are coordinated by calcium ions. The outer surfaces of these coordinated SiO_4^{2-} chains are balanced by water molecules and hydrogen bonds to form a stable crystal structure of sandwich-like layers. Jennite has a similar structure to that of tobermorite, despite their differences, such as different calcium to silicon ratios and the number of bridging oxygen atoms in the center layer. Silicon oxide tetrahedron chains are generally described using the Q^n format, where n is the number of oxygen atoms (usually 1–4) shared by $n + 1$ tetrahedrons. Zhou *et al.* [12] built the tobermorite-like C–S–H models by molecular dynamics simulation and achieved that the Q^2 tetrahedron is consistent with the measured ^{29}Si magic angle spinning (MAS) nuclear magnetic resonance (NMR) experiments.

As discussed, SiO_4^{2-} chains form the main structure of basic C–S–H units. Accordingly, bonding between these chains can be expected to affect the stacking of basic C–S–H units. Zhu *et al.* [13] described that the SiO_4^{2-} chains are mainly connected by covalent bonds. Sun *et al.* [14] researched the modification of SiO_4^{2-} covalent bonds by amine. While the SiO_4^{2-} chains are evaluated by recent scholars, considerable speculation remains regarding the bonding between mutually stacked C–S–H units. The aggregation of C–S–H particles is generally assumed to be governed by the sum of electrostatic forces, van der Waals forces, and capillary forces. This may result in that the mechanical strength and toughness of C–S–H are less than those of SiO_4^{2-} ceramic materials involving much stronger covalent bonding and more extensive tetrahedron chain networks [13]. This cannot completely exclude the possibility of other structures existing between the aggregation of C–S–H particles. Recent studies have revealed that the tobermorite-like and jennite-like C–S–H are predominantly composed of Q^2 SiO_4^{2-} chains. Tang and Chen [15] have demonstrated that Q^2 tetrahedron chains represent relative content of 40–70% of the mass in C–S–H samples. Moshiri *et al.* [16] found that the relative content of Q^2 chains of C–S–H is 48.0%. Theoretically, covalent bonding interactions between Q^2 tetrahedron chains in C–S–H could mitigate the disadvantages of C–S–H, such as its low toughness. Zhou *et al.* [17] demonstrated the potentially beneficial effects of the reorganization of Q^2 chains at the nanoscale and mesoscale which indirectly indicate for C–S–H modified with polyaniline. In addition, the Q^2 tetrahedron chains in C–S–H have been the subject of considerable research. For example, Abdolhosseini Qomi *et al.* [18] described that the spatial distribution of Q^2 tetrahedron chains in C–S–H has been demonstrated to be nonuniform, and the lengths of these chains decreased with an increase in the Ca/Si ratio. The experiment by Gardner *et al.* [19] indicated that Raman specturm was a useful method to monite the SiO_4^{2-} covalent bonds of Q^2 tetrahedron chains. It is noteworthy that a fuller appraisal of the role of Q^2 tetrahedron chains in the stacking of C–S–H particles requires detailed information regarding the chemical bonds of each C–S–H nanograins, possible connection between stacked C–S–H particles and the characteristics of Q^2 tetrahedron chains at the nanoscale.

Recent studies have revealed the nanostructure of C–S–H, including crystalline and gel models, types of C–S–H crystal units, and Q^2 tetrahedron chains. However, the evaluation about the real ratios of different C–S–H crystal units of 30–100 nm C–S–H stacking particles as well as experimental information of nanoscale chemical bonds distribution of Q^2 tetrahedron chains is still lacking.

The above-discussed issues can be potentially evaluated by applying the atomic force microscopy-infrared spectroscopy (AFM-IR) technique, which is a new method that combines AFM and Fourier transform IR (FTIR) spectroscopy to obtain local detailed structural information at the nanoscale [20]. For example, AFM-IR has been applied for observing the chemical bonds of polymer films *in situ*, which was researched by Dazzi *et al.* [21], and the protein distributions of a virus, which was revealed by Dou *et al.* [22], at a 100 nm scale. The standard FTIR spectroscopy process relies on the optical absorbance of a sample surface to determine the characteristic chemical bonds of the material based on the wavelength of the incident IR radiation. However, this is a technique suitable only for bulk material samples. In contrast, AFM can map the topography of a sample surface at a spatial resolution of about 10 nm based on minute deflections in the cantilever of the AFM probe. The AFM-IR technique combines these two methods, and applies a mechanism denoted as resonance-enhancement to increase the spatial resolution of FTIR spectroscopy to that of AFM. Zhou [23] pointed that this mechanism relies on the fact that the absorption of IR radiation will produce local instantaneous heating at the sample surface, which can be detected by AFM according to the corresponding surface deformation. Gourion-Arsiquaud *et al.* [24] believed that the high localization of this heating signal is guaranteed because only the IR absorbance of the sample surface near the tip of the AFM probe makes a significant contribution to the AFM-IR signal owing to the fact that the amplitude of the high-frequency vibration of the AFM tip is sensitive to the speed of the surface displacement, rather than the displacement itself. Accordingly, any disturbance registered by the AFM probe depends entirely upon the chemical bonds absorbing the incident IR radiation, which then provides a nanoscale mapping of the material bonds at the sample surface. This makes AFM-IR ideally suited for identifying the characteristic IR absorbance peaks associated with the Si–O–Si bonds of Q^2 tetrahedron chains, which occur in the wavenumber range of 900–1,200 cm^{-1} [25].

The present work evaluates the above-discussed issues by applying the AFM-IR technique to investigate the chemical bonds and units of C–S–H nanoparticles. The AFM-IR spectra captured at isolated points on the surface of C–S–H samples are analyzed by deconvolution to determine the relative proportions of Q^2 tetrahedron chains associated with tobermorite-like and jennite-like nanocrystals. This AFM-IR deconvolution provides a method to obtain the details of mixture at nanoscale. The orientations of Q^2 tetrahedron chains between C–S–H gel particles are analyzed by mapping the distribution of Q^2 tetrahedron chain orientations within a 400 nm × 400 nm area of C–S–H sample surfaces, and the distribution of the missing region of Q^2 chains is also analyzed. In addition, the possible connection between C–S–H particles is also analyzed. These findings enhance our understanding of the stacking of C–S–H particles, and provide detailed guidance for efforts related to C–S–H modification.

2 Materials and methods

2.1 Synthesis of C–S–H samples

The C–S–H samples were synthesized by mixing aqueous hydrated sodium silicate ($Na_2SiO_4·9H_2O$; Sigma-Aldrich, ≥98%) and hydrated calcium nitrate ($Ca(NO_3)_2·4H_2O$; Sigma-Aldrich, 99%) solutions. The concentrations of the prepared aqueous solutions were fixed at 0.2 M. The molar Ca/Si ratio was 1.0 [26]. In the mixing process, the calcium nitrate solution was added to the sodium silicate solution (completing within 180 s) under stirring, and a white precipitate was formed immediately. The sample was cured at 50°C for 28 days under stirring. Then, the white precipitate powder was washed twice with deionized water and dried at 50°C (Figure 1).

2.2 AFM-IR

The C–S–H samples employed for AFM-IR testing were C–S–H tablets subjected to polishing treatment. C–S–H

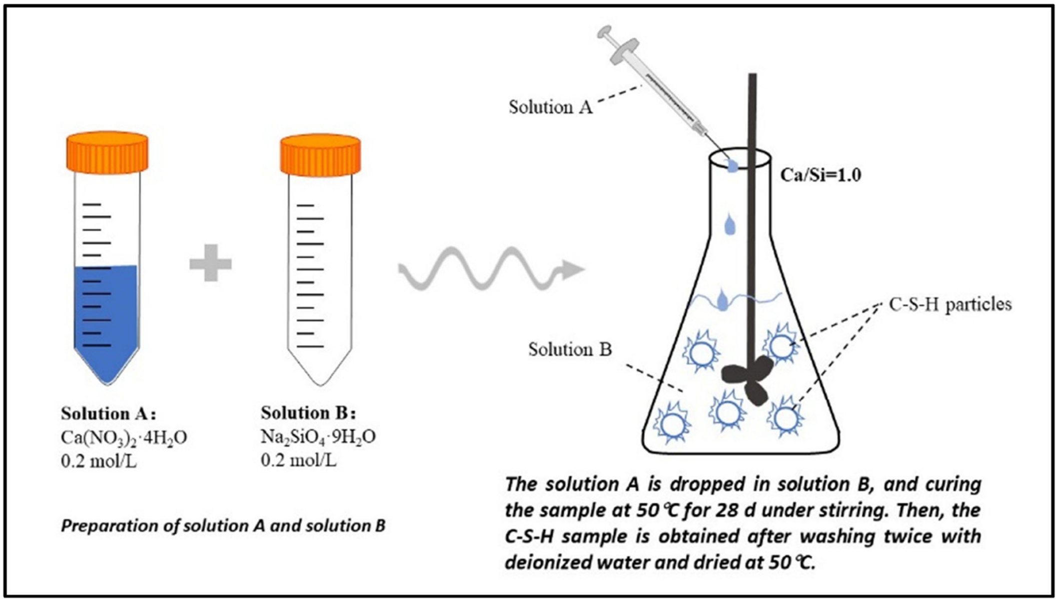

Figure 1: Schematic diagram of the preparation process of C–S–H samples.

tablets were vacuum impregnated with epoxy resin and cured at 25°C [5]. These cured samples were then progressively grinded and polished with SiC paper and diamond wheels [6]. In order to prevent the introduction of impurities, no polishing liquid was used. All AFM-IR testing was conducted using a NanoIR2 system (Bruker). The individual IR absorbance peaks in the 900–1,200 cm^{-1} band were obtained by deconvolution based on Gaussian functions. The most prominent IR absorption peak characteristic of Si–O–Si bonds in Q^2 tetrahedron chains occurs at 980 cm^{-1} [25]. Therefore, we conducted AFM-IR mapping based on the intensity of IR absorbance at 980 cm^{-1} to evaluate the spatial distribution of Q^2 chains. The contact resonance frequency was adjusted in real time.

2.3 Other characterization techniques

The crystalline structure of the C–S–H samples was investigated based on X-ray diffraction (XRD) data obtained using a D8 ADVANCE powder diffractometer (Bruker) with graphite-monochromatized Cu-Kα radiation (K = 1.5406 Å) generated at an acceleration voltage of 40 kV and a beam current of 40 mA. Step scanning was conducted in the 2θ range of 5°–70° with a scan step of 0.02°. We also obtained detailed information regarding the SiO_2 Q^2 tetrahedron chains of the C–S–H samples based on ^{29}Si MASNMR spectroscopy experiments conducted using a DD2 600 MHz spectrometer (Agilent) at a resonance frequency of 119.23 MHz. We recorded ^{29}Si cross polarization (CP) NMR spectra using a 4 mm probe with a spinning rate of 15 kHz at room temperature. All ^{29}Si CP-MAS NMR spectroscopy experiments were conducted with a delay time of 3 s and a contact time of 1 ms using 5,000 scans. These results were also subjected to deconvolution based on Gaussian curves. Talos F200X G2 was used for transmission electron microscopy (TEM) test. The accelerating voltage was 200 kV, and a very low electron beam current were selected.

3 Results

3.1 Characterization of synthesized C–S–H

The XRD results obtained for a representative synthesized C–S–H sample are shown in Figure 2, and the results are compared with the standard tobermorite and jennite XRD peak characteristics. As shown, the d-spacing values associated with tobermorite peaks (PDF# 83-1520) are 1.139, 0.308, 0.281, 0.183, and 0.167 nm, while the d-spacing values associated with jennite peaks (PDF# 18-1206) are 1.050, 0.304, 0.278, 0.183, and 0.168 nm. The XRD results obtained for C–S–H exhibit d-spacing values of around 1.051–1.145, 0.304–0.306, 0.279–0.282, 0.183, and 0.167 nm, which are consistent with previously reported results [27]. Accordingly, the d-spacing values obtained for the C–S–H sample are consistent with those of tobermorite and jennite [28]. Moreover, XRD peaks associated

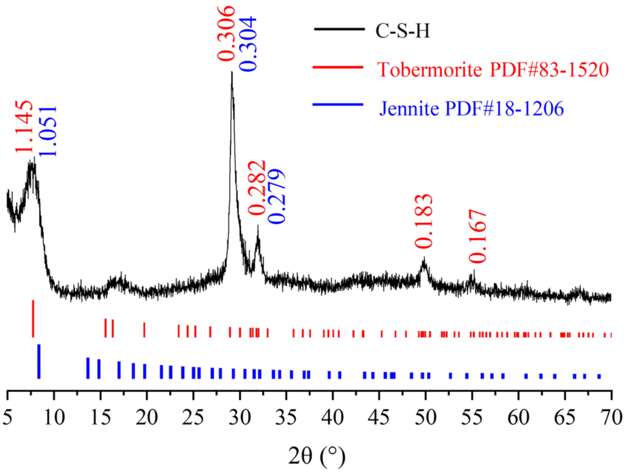

Figure 2: XRD spectra of a representative synthesized C–S–H sample, and the basic *d*-spacing peak characteristics of tobermorite and jennite.

with calcium carbonate and calcium hydroxide are not observed, indicating that these materials do not form in the synthesis process. Therefore, we can conclude that the crystalline structure of the synthesized C–S–H sample was tobermorite-like and jennite-like, and that the basic C–S–H units are tobermorite-like and jennite-like nanocrystals.

The ^{29}Si CP-MAS NMR spectroscopy results obtained for a representative synthesized C–S–H sample are presented in Figure 3 along with the results of peak deconvolution. The chemical shift of ^{29}Si depends on adjacent atoms in the local environment. Accordingly, the chemical shift peaks at −84.4 and −88.5 ppm are assigned to Q^2 tetrahedron chains [29]. And the chemical shift peaks at −92.7 ppm is assigned to Q^3 chains [30]. We note that two types of Q^2 chains are observed with different chemical shifts, and the Q^2 chains in the C–S–H sample account for a very high percentage of 69.2% + 13.7% = 82.9% of the total area of the chemical shift signal. In light of the XRD results, these peaks associated with Q^2 chains in the C–S–H sample can be attributed to the tobermorite-like and jennite-like nanocrystals of C–S–H. This is also supported by the ^{29}Si CP-MAS NMR spectroscopy results obtained for tobermorite and jennite [31]. The chemical shift peaks at −84.4 and −88.5 ppm cannot be specifically related explicitly to tobermorite and jennite [32]. Chiang and Chang [33] demonstrate that the Q^2 tetrahedron can be divided into bridging tetrahedra and paired tetrahedra vacancies in dreierketten chains. Li *et al.* [34] revealed that strong hydrogen bonds are favored to form in C–S–H with high Ca/Si molar ratios. Thus, the chemical shifts associated with the Q^2 sites in both tobermorite and jennite vary at different spatial positions, which are consistent with the observation of Maeshima *et al.* [35]. Moreover, defects in the Q^2 chains of C–S–H induce differences in the chemical shifts observed for C–S–H from those observed for tobermorite and jennite. Nonetheless, the XRD and NMR spectroscopy results concurrently demonstrate that the C–S–H samples mainly consist of the Q^2 chains of tobermorite-like and jennite-like nanocrystals, and the 17.1% of the NMR signal attributed to Q^3 chains.

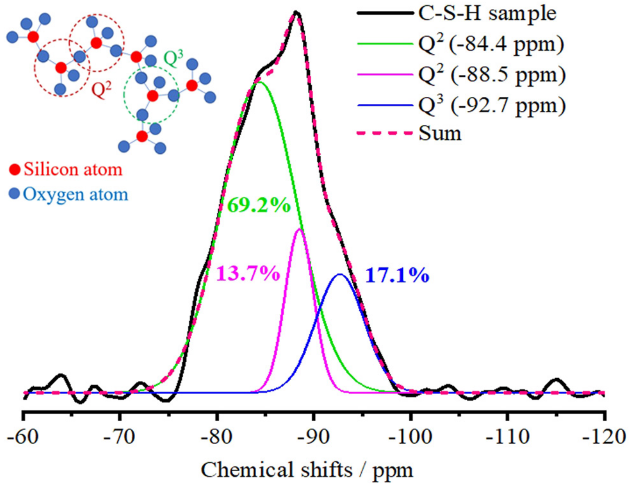

Figure 3: ^{29}Si CP-MAS NMR spectroscopy results obtained for a representative synthesized C–S–H sample along with the results of chemical shift peak deconvolution.

The TEM photographs of prepared C–S–H are presented in Figure 4. In Figure 4(a) and (b), it can be obviously observed that the C–S–H was foil-like morphology. Kapeluszna *et al.* [36] observed this thin, crumpled foils in C–S–H with the Ca/Si ratio of 1.0. Kong *et al.* [37] found nanoparticle size of the C–S–H gels with the same foils. The XRD analysis in our research demonstrated that C–S–H contains the crystal units. To obtain more information of these units, electron diffraction of the selected area is performed in the red circular area of Figure 4(b) and the results of the polycrystalline ring can be observed in Figure 4(c). This indicates that the C–S–H consists of nanocrystal aggregates. In Figure 4(d), the observed crystal unit is about 5–7 nm. The TEM analysis demonstrates the existence of crystal units in synthesis C–S–H samples, which is consistent with XRD results and current reference.

A representative AFM image of a 400 nm × 400 nm surface area of a C–S–H sample is presented in Figure 5. The figure indicates the presence of distinct C–S–H gel particles numbered 1–6 with clear boundaries that are around 20–30 nm in diameter. Jennings established a nanogel model of C–S–H that considered C–S–H to be formed from the stacking of 2 nm gel particles into 5.6 nm basic gel units, which are in turn stacked to form the final gel structure [6]. From this perspective, the six C–S–H gel

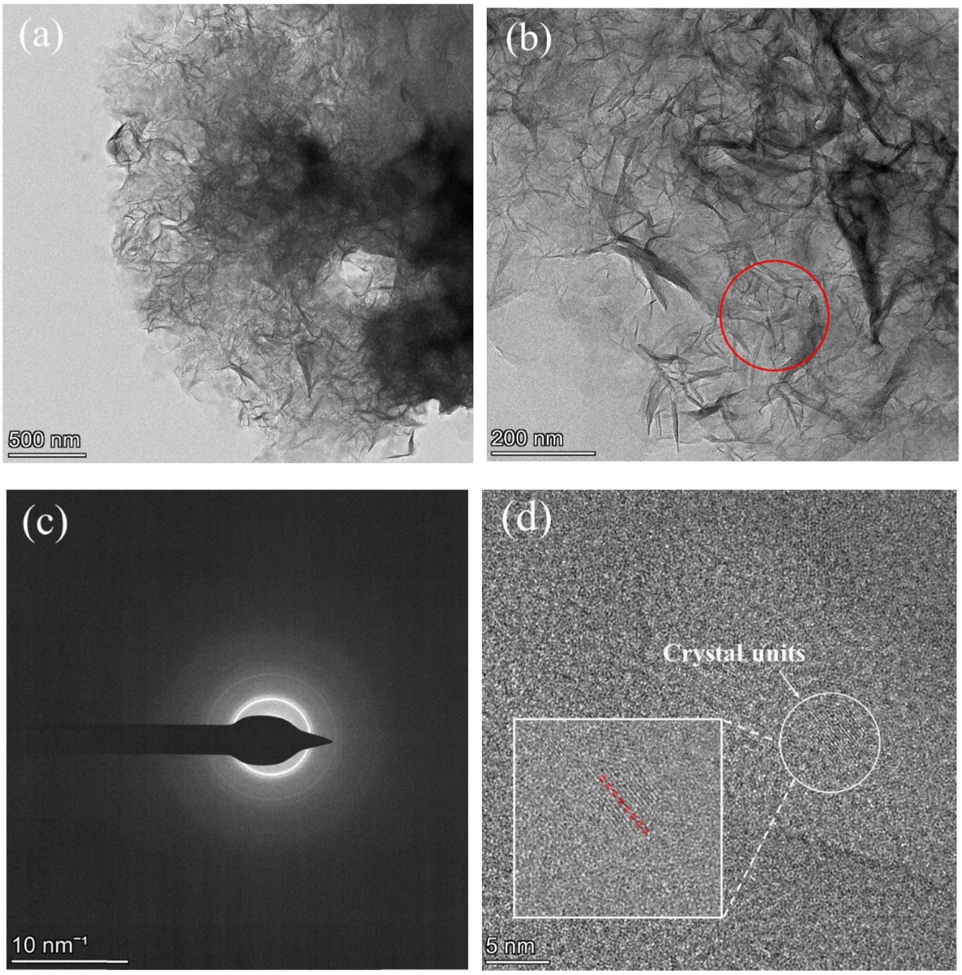

Figure 4: TEM photographs for the prepared C–S–H. (a) and (b) foil-like C–S–H morphology, (c) electron diffraction of selected area in red circular area in (b), and (d) 5–7 nm crystal unit.

particles with diameters of 20–30 nm in Figure 3 consist of 4–5 basic 5.6 nm-diameter gel units or 10–15 stacked 2 nm-diameter gel particles. In contrast, the CM-II model [7] considers C–S–H to be formed from the stacking of basic tobermorite-like or jennite-like nanocrystal units with diameters of 3–6 nm. From this perspective, the six C–S–H gel particles in Figure 3 consist of 5–10 basic nanocrystal units. Both models believe that 30–60 nm particles observed in Figure 3 are not the basic units of C–S–H. Considering the XRD and NMR results, the CM-II model was adopted here for analyzing the nanostructure of C–S–H.

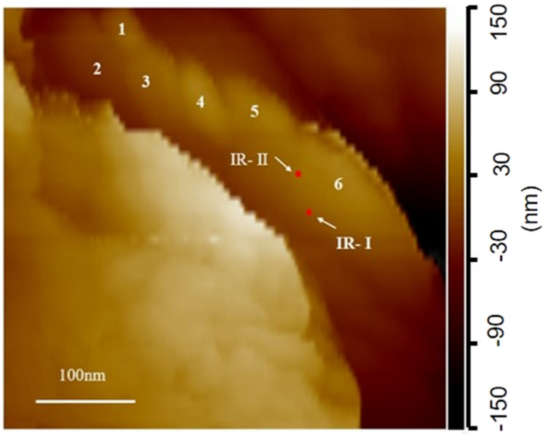

Figure 5: AFM image of a 400 nm × 400 nm surface area of a representative C–S–H sample along with distinct C–S–H gel particles numbered 1–6 and points of AFM-IR spectra collection denoted as IR-I and IR-II.

3.2 Nanocrystal-like structure of C–S–H

The structure of C–S–H nano-particle 6 in Figure 5 was evaluated *in situ* by AFM-IR at the points labeled IR-I and IR-II in the figure, and the corresponding AFM-IR spectra are presented in Figure 6, along with the results of deconvolution in the IR absorbance band between 900 and 1,200 cm^{-1}. The distance between points IR-I and IR-II is only about 35 nm. Nonetheless, the deconvolution results differ substantially. The stretching vibration of 900–1,200 cm^{-1} can be attributed to Q^2 tetrahedron of C–S–H [25]. The results in Figure 6(a) for IR-I indicate that three absorbance peaks were obtained by deconvolution at 971.8, 1038.2, and 1,172.3 cm^{-1}, which are all assigned to tobermorite-like Q^2 tetrahedron chains, and one absorbance peak was obtained at 1107.0 cm^{-1}, which is assigned to jennite-like Q^2 tetrahedron chains [38]. The results in Figure 6(b) for IR-II indicate that three absorbance peaks were obtained by deconvolution at 951.8, 1006.7, and 1127.4 cm^{-1}, which are all assigned to tobermorite-like Q^2 tetrahedron chains, and two absorbance peaks were obtained at 1102.0 and 1060.9 cm^{-1}, which are assigned to jennite-like Q^2 tetrahedron chains [38]. These results indicate that the nanoscale crystal structure of C–S–H differs substantially at IR-I and IR-II. These structural differences in the Q^2 tetrahedron chains of C–S–H can be characterized according to the relative areas under the deconvolved peaks associated with tobermorite-like and jennite-like crystal structures relative to the total area, and the ratio (T/J) of the total peak areas associated with tobermorite-like and jennite-like crystal structures. These deconvolution results are listed in Table 1 for the spectra obtained at points IR-I and IR-II. These results indicate that the proportions of areas associated with tobermorite-like and jennite-like units at IR-I were 84.5 and 15.6% of the total peak area, respectively, which resulted in a large T/J ratio of 5.41. In contrast, the proportions of areas associated with tobermorite-like and jennite-like units at IR-II were 65.3 and 34.7% of the total peak area, respectively, which resulted in a smaller T/J ratio of 1.88. It is obvious that both points IR-I and IR-II were dominated by tobermorite-like crystal units, although this dominance was much greater at IR-I than at IR-II. These observations indicate that C–S–H nanograins have a highly complex nano-structure consisting of different types of nanocrystals, and the relative quantity of tobermorite-like and jennite-like units in C–S–H nanograins can be analyzed by AFM-IR

3.3 Stacking of C–S–H particles

The stacking orientation of layered minerals has an important effect on their mechanical performance. For example, pearls are formed from layers of calcium carbonate, which help in increasing the toughness of the shell [39]. This suggests that the ordered assembly of nanocrystal-like C–S–H units would be conducive to improving the toughness of the material. From this perspective, the orientation of the SiO_2 Q^2 tetrahedron chains in C–S–H gel particles can be expected to have an impact on the mechanical properties of the particles [40]. Therefore, understanding the orientation of Q^2 chains in C–S–H is a prerequisite for studying the means of enhancing cement toughness by guiding the formation of the Q^2 chain-layered sequence.

Previous studies have demonstrated that stacked C–S–H particles are restricted to small diameters. For example, C–S–H particles were found to be restricted to particle diameters of about 30–60 nm by AFM [15] and 10–30 nm by TEM [36,41]. This restriction has been attributed to the obviously self-limiting growth of C–S–H microcrystals,

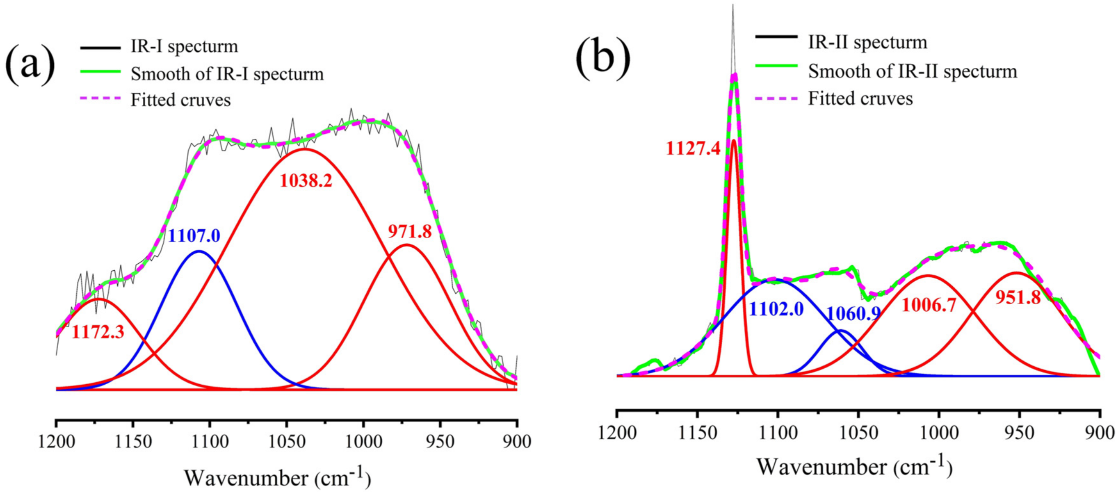

Figure 6: AFM-IR spectra collected at positions (a) IR-I and (b) IR-II along with the results of band deconvolution.

Table 1: Deconvolution results of tobermorite-like and jennite-like nanocrystals in C–S–H based on Figure 6

Position in Figure 3	Tobermorite-like units			Jennite-like units		T/J ratio
Peak at IR-I (cm^{-1})	971.8	1038.2	1172.3	1107.0		5.41
Proportion of total area (%)	18.6	54.9	11.0	15.6		
Peak at IR-II (cm^{-1})	951.8	1006.7	1127.4	1102.0	1060.9	1.88
Proportion of total area (%)	27.5	28.4	9.4	28.9	5.8	

which makes it impossible for growth to progress into large-scale crystals. The growth of C–S–H microcrystals is mainly driven by physical surface force that facilitates the mutual aggregation of nanocrystals. However, the potential existence of covalent connection between C–S–H particles remains unclear.

These issues associated with the orientation of Q^2 tetrahedron chains and stacking in C–S–H particles were investigated by conducting AFM-IR mapping of the region of the C–S–H sample shown in Figure 5. These mapping results are presented in Figure 7(a), and the mapping results obtained at greater resolution for the region associated with C–S–H gel particles numbered 1–6 are presented in Figure 7(b). Here the color scales represent the intensity of the signals associated with Q^2 tetrahedron chains at 980 cm^{-1}, as measured in mV, where all colors from light yellow (0 mV) to red (6 mV) represent the presence of Q^2 tetrahedron chains, and brown (≤6 mV) represents microcracks.

As shown in Figure 7(a), the six C–S–H gel particles identified solely by AFM in Figure 5 can be more accurately identified as seven gel particles according to the AFM-IR mapping results of the region, which provide superior information for distinguishing boundary regions between C–S–H gel particles. The detailed information shown in Figure 7(b) indicates that the chemical bonds associated with Q^2 chains also exist between stacked C–S–H gel particles. This is particularly evident between the cluster of particles numbered 1–3, between the bridging particle 4 and particles 3 and 7, and between the cluster of particles 5–7. This indicates that Q^2 chains participate in the C–S–H gel particle stacking process. Nonetheless, green and blue areas are also clearly observable in the boundaries between the gel particles. These areas can be attributed to the missing of Q^2 chains with high concentrations, and their positions at the particle boundaries correspond to the particle boundaries observed by AFM in Figure 5.

The orientations of the connective and the missing region of Q^2 chains observed in the particle boundaries of Figure 8(a) were evaluated statistically according to AFM-IR mapping results. This area was selected for analysis owing to the greater density of connective Q^2 chains than that observed in Figure 7(a). Here connective Q^2 chains are assigned to IR absorbance intensities at 980 cm^{-1} that are greater than 2 mV and the missing region of Q^2 chains are assigned to intensities less than or equal to −1 mV. One example is shown in Figure 8(b), which is the area A marked in Figure 8(a). This selection of high intensity signals can avoid statistical errors caused by insufficient signal strength. The AFM-IR mapping results present pixel clusters that are rod-like in appearance, and the prevailing

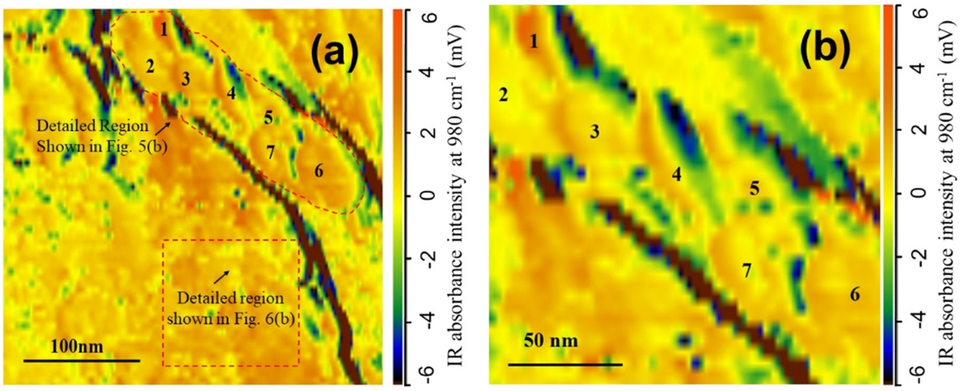

Figure 7: AFM-IR mapping results for the region shown in Figure 3: (a) entire region; (b) magnified region associated with C–S–H gel particles numbered 1–6.

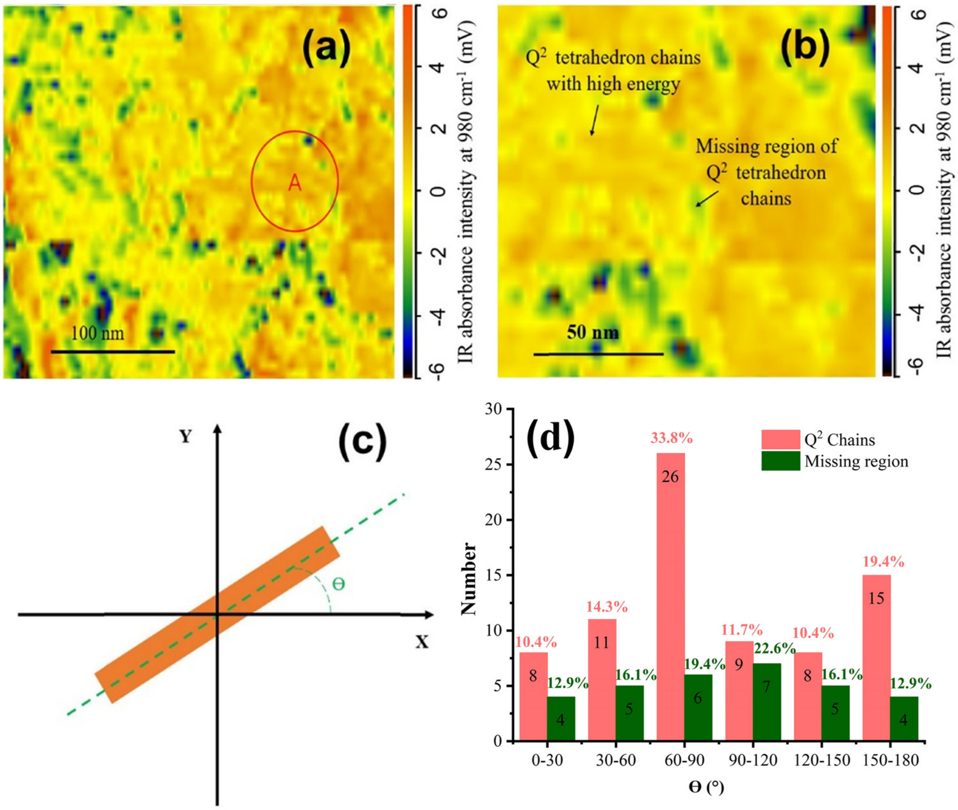

Figure 8: AFM-IR mapping results for a separate region near that shown in Figure 5(a): (a) entire region; (b) magnified region associated with the region marked in Figure 5(a) (c) Illustration of the orientation of connective and the missing region of Q^2 chains based on an angle θ in the range of 0–180°; (d) Distributions of connective and the missing region of Q^2 chain orientations in Figure 6(a).

color of these clusters are therefore indicative of connective and the missing region of Q^2 chains. Here we consider only pixel clusters with an aspect ratio greater than 1.5 to eliminate non-rod-like shapes from the statistical results. The data was statistically analyzed by Analysis Studio® software, which can provide the absorbance intensities and measure size (accuracy, 0.01 nm). This yielded 77 pixel clusters indicative of connective Q^2 chains and 31 pixel clusters indicative of the missing region of Q^2 chains. The definition of the orientation angle θ applied in the statistical analysis is illustrated in Figure 8(c), and its range is 0–180°. The results obtained for the various pixel clusters are presented in Figure 8(d). For connective Q^2 chains, the results indicate that the highest proportion of orientations (33.8%) are found with θ values in the range 60–90°, while the orientation range 150–180° has the next highest proportion (19.4%), the orientation range 30–60° is third (14.3%), and the remaining orientation categories account for about 10% each of the total number of connective Q^2 chains. This indicates that the orientation of the detected connective Q^2 chains was not evenly distributed over the examined region. In contrast, the orientations of the missing region of Q^2 chains were far more uniformly distributed, with all orientation categories accounting for between about 13% and 23% of the total number of missing regions.

4 Discussion

The orientation concentration of Q^2 chains in example regions was discussed. Theoretically, a preferred alignment of connective Q^2 chains would result in different mechanical performances for C–S–H samples with respect to that preferred direction. However, Zhu *et al.* [6] demonstrated that C–S–H particles (not units) is an isotropic material. It is noteworthy that there are various preparations of C–S–H, which does not affect the isotropic properties. This may be related to the random alignment of the missing region of Q^2 chains within the C–S–H particle boundaries, which would tend to enforce isotropy. Of course, the AFM-IR mapping results presented here cannot confirm the nature of the missing region, although the NMR spectroscopy results suggest that the missing regions are likely to be Q^3 chains. Nevertheless, the existence of Q^0, Q^1, and nanopores in these areas cannot be ruled out. This is because NMR signals require more atoms of Q^0 and Q^1 spinning in the same state to obtain the signal.

The observed orientation concentration of connective Q^2 chains around Θ values of 60–90° may be related to the formation process of C–S–H. In this regard, we note that Krautwurst *et al.* [42] postulated that C–S–H is formed through a heterogeneous nucleation process, where the C–S–H precursor is first formed and then the precursor forms nanocrystal-like C–S–H particles. This conceptualization is consistent with non-static crystallization theory. In contrast, amorphous crystallization theory postulates that the precursor is in an amorphous phase that includes structural fragments similar to the long cured crystals [43]. These structural fragments in the C–S–H precursor induce the formation of crystalline phases, which represent the so-called active sites. According to the heterogeneous nucleation process of C–S–H, these active sites will induce the formation of nanocrystal-like C–S–H particles. Therefore, it is reasonable to speculate that the direction of Q^2 chain growth may be related to the active sites in the structural fragments of the C–S–H precursor. It is necessary to mention that the statistical results of mesoscale regions (≥1,000 nm) may not be conformable to this research. The reason is that the statistic regions in this research are composed of nanocrystal-like C–S–H units, which characters as short-range order structures. And the mesoscale regions are related to long-range disordered C–S–H structure. In addition, it is worthy to note that the statistical data is related with a limited number of experiments.

The C–S–H is the source of Portland cement strength. The modification of C–S–H can make up the defects of C–S–H. Meng *et al.* [41] found the attachments of nano-SiO_2 aggregates on the surface of the C–S–H gel. Poor toughness is one of the defects of Portland cement, and the cause of this can be closely related to the stacking structure of C–S–H particles. Efforts to address this issue generally involve C–S–H modification on mesoscopic and nanometer scales. For example, Sun *et al.* [44] prepared a cement-based absorbing board with perfectly mechanical–electrical–magnetic properties by designing the mesoscopic structure. One of the further property enhancement method for this cement-based absorbing board is related to the C–S–H modification at nanoscale. There are some methods to enhance the strength of cement. The hot-focus is modifying C–S–H nanostructure by tailoring the pressure, temperature, water content, and adding polymers [45] such as polyvinyl alcohol, protein, *etc*. These modifications are guided by the gel model or crystalline model. The Q^2 chains which act as bridges between C–S–H particles provide the modifying object to enhance the toughness of the C–S–H. In this respect, if the polymer inserting C–S–H plays as the “bridging Q^2 chains” between C–S–H particles, the toughness of C–S–H aggregates should become better. The other contributions to cement chemistry are to supplement the experiment information for CM-II models, such as T/J ratios with 50 nm and chemical bonds of C–S–H gaps. Therefore, the results of this article are useful for providing basic theoretical guidance for C–S–H modification and cement toughness enhancement. However, the activity of the C–S–H precursor in the formation of Q^2 chains requires further detailed exploration. The AFM-IR provides a method to obtain the nanostructure of C–S–H successfully. Actually, there is another similar testing method called tip-enhanced Raman spectroscopy (TERS), which combinate AFM and Raman spectroscopy. TERS needs the detected object to have detection activity, and the C–S–H needs to be verified or enhanced. Despite this, the realization about the *in situ* detection of AFM-IR and TERS will provide more structural details of the cement-based materials. In addition, some hypothesis for cement chemistry is still hard to be certified by the limitation of obtaining *in situ* nanoscale information, although they are accepted by many scholars. AFM-IR is a powerful *in situ* method to evaluate the hypothesis in cement chemistry at nanoscale.

5 Conclusion

The aggregation of C–S–H particles forms a complex nanoscale structure, which determines the mechanical performance of cement. This aggregation is generally assumed to be governed by physical surface force. The possible existence of chemical bonding between C–S–H particles other than that governed by physical surface force is controversial. The present work applied the AFM-IR technique to an investigation of the stacking of C–S–H nanocrystals. The results demonstrated that the relative quantity of tobermorite-like and jennite-like units in C–S–H nanograins can be analyzed by AFM-IR. The ratios of tobermorite-like and jennite-like C–S–H crystals varied at different points within the nanoscale regions of a C–S–H sample. The results of AFM-IR spatial mapping revealed the existence of Q^2 chains acting as bridges between C–S–H particles and the presence of the missing region of Q^2 chains within the C–S–H particles or at their boundaries. In addition, the orientations of both connective and the missing region of Q^2 chains were analyzed statistically.

The orientations of connective Q^2 chains were found to be unevenly distributed at short range, while the orientations of the missing region of Q^2 chains were found to be randomly distributed. The results are useful for providing basic theoretical guidance for C–S–H modification and cement enhancement.

Funding information: This work was supported by the National Natural Science Foundation of China [Grant No. 51772212 and 51108341], National Key R&D Program of China [Grant No. 2019YFC1906203].

Author contributions: All authors have accepted responsibility for the entire content of this manuscript and approved its submission.

Conflict of interest: The authors state no conflict of interest.

References

[1] Rostami R, Klemm AJ, Almeida FCR. Reduction of shrinkage by Superabsorbent polymers (SAP) in fibre reinforced mortars. Constr Build Mater. 2021;288:123109.

[2] Bae S, Taylor R, Shapiro D, Denes P, Joseph J, Celestre R, et al. Soft X-ray ptychographic imaging and morphological quantification of calcium silicate hydrates (C–S–H). J Am Ceram Soc. 2015;98(12):4090.

[3] Hou D, Yang Q, Wang P, Jin Z, Wang M, Zhang Y, et al. Unraveling disadhesion mechanism of epoxy/CSH interface under aggressive conditions. Constr Build Mater. 2021;146:106489.

[4] Papatzani S, Paine K, Calabria-Holley J. A comprehensive review of the models on the nanostructure of calcium silicate hydrates. Constr Build Mater. 2015;74:219.

[5] Zhu X, Qian C, He B, Chen Q, Jiang Z. Experimental study on the stability of C–S–H nanostructures with varying bulk CaO/SiO_2 ratios under cryogenic attack. Cement Concrete Res. 2020;135:106114.

[6] Zhu X, Jiang Z, He B, Qian C. Investigation on the physical stability of calcium-silicate-hydrate with varying CaO/SiO_2 ratios under cryogenic attack. Constr Build Mater. 2020;252:119103.

[7] Yang J, Zhang W, Hou D, Zhang G, Ding Q. Structure, dynamics and mechanical properties evolution of calcium silicate hydrate induced by dehydration and dehydroxylation. Constr Build Mater. 2021;291:123327.

[8] Hou D, Zhang W, Wang P, Wang M, Zhang H. Mesoscale insights on the structure, mechanical performances and the damage process of calcium-silicate-hydrate. Constr Build Mater. 2021;287:123031.

[9] Polisi M, Vezzalini MG, Bonaccorsi E, Biagioni C, Arletti R. High pressure behaviour of tobermorite supergroup minerals: an in situ synchrotron X-ray powder diffraction study. Cement Concrete Res. 2020;138:106249.

[10] Huang J, Fan Y, Ouyang X, Han Q. Molecular dynamics study on axial mechanical properties of calcium silicate hydrate. Mater Res Express. 2020;7(8):085011.

[11] Zhou J, Liang Y. Effect of water on the dynamic tensile mechanical properties of calcium silicate hydrate: based on molecular dynamics simulation. Materials. 2019;12:2837.

[12] Zhou Y, Tang L, Liu J, Miao C. Interaction mechanisms between organic and inorganic phases in calcium silicate hydrates/poly (vinyl alcohol) composites. Cement Concrete Res. 2019;125:105891.

[13] Zhu Z, Wang Z, Zhou Y, Wei Y, She A. Synthesis and structure of calcium silicate hydrate (C–S–H) modified by hydroxyl-terminated polydimethylsiloxane (PDMS). Constr Build Mater. 2021;267:120731.

[14] Sun D, Yan J, Ma X, Lan M, Wang Z, Chen Z, et al. On the characterization of amine molecules behaviors in the nanochannels forming in calcium silicate hydrate gel. Appl Surf Sci. 2021;560:149994.

[15] Tang Y, Chen W. Effect of magnesium on the structure and chemical composition of calcium silicate hydrate at elevated temperature. Constr Build Mater. 2020;240:117925.

[16] Moshiri A, Stefaniuk D, Smith SK, Morshedifard A, Rodrigues DF, Qomi M, et al. Structure and morphology of calcium-silicate-hydrates cross-linked with dipodal organosilanes. Cement Concrete Res. 2020;133:106076.

[17] Zhou Y, She W, Hou D, Yin B, Chang H, Jiang J, et al. Modification of incorporation and in-situ polymerization of aniline on the nano-structure and meso-structure of calcium silicate hydrates. Constr Build Mater. 2018;182:459.

[18] Abdolhosseini Qomi MJ, Krakowiak KJ, Bauchy M, Stewart KL, Shahsavari R, Jagannathan D, et al. Combinatorial molecular optimization of cement hydrates. Nat Commun. 2014;5(1):4960.

[19] Gardner DW, Li J, Kunz M, Zhu C, Monteiro P, Maboudian R, et al. Plastic deformation mechanism of calcium-silicate hydrates determined by deviatoric-stress Raman spectroscopy. Cement Concrete Res. 2021;146:106476.

[20] Luo H, Xiang Y, Tian T, Pan X. An AFM-IR study on surface properties of nano-TiO_2 coated polyethylene (PE) thin film as influenced by photocatalytic aging process. Sci Total Environ. 2021;757:143900.

[21] Dazzi A, Saunier J, Kjoller K, Yagoubi N. Resonance enhanced AFM-IR: A new powerful way to characterize blooming on polymers used in medical devices. Int J Pharm. 2015;484(1):109.

[22] Dou T, Li Z, Zhang J, Evilevitch A, Kurouski D. Nanoscale structural characterization of individual viral particles using atomic force microscopy-infrared spectroscopy (AFM-IR) and tip-enhanced Raman spectroscopy (TERS). Anal Chem. 2020;92(16):11297.

[23] Zhou H. Chapter 2 – advanced spectroscopic technique for the study of nanocontainers: atomic force microscopy-infrared spectroscopy (AFM-IR). Smart Nanocont [Internet]; 2020 Jan [cited 2020 Jan 24]. [about 10p]. Available from: doi: 10.1016/B978-0-12-816770-0.00002-2.

[24] Gourion-Arsiquaud S, Marcott C, Hu Q, Boskey AL. Studying variations in bone composition at nano-scale resolution: a preliminary report. Calcif Tissue Int. 2014;95(5):413.

[25] Yu P, Kirkpatrick RJ, Poe B, McMillan PF, Cong X. Structure of calcium silicate hydrate (C–S–H): Near-, mid-, and far-infrared spectroscopy. J Am Ceram Soc. 1999;82(3):742.

[26] Pellenq RJ, Kushima A, Shahsavari R, KJVanVliet, Buehler MJ, Yip S, et al. A realistic molecular model of cement hydrates. Proc Natl Acad Sci USA. 2009;106(38):16102.

[27] Maddalena R, Li K, Chater PA, Michalik S, Hamilton A. Direct synthesis of a solid calcium-silicate-hydrate (C–S–H). Constr Build Mater. 2019;223:554.

[28] Grangeon S, Claret F, Linard Y, Chiaberge C. X-ray diffraction: a powerful tool to probe and understand the structure of nanocrystalline calcium silicate hydrates. Acta Crystallogr B. 2013;69:465.

[29] Chiang Y, Chang SW. Bridging the gap between NMR measured mean silicate chain length and nano-scale silicate polymorphism of calcium silicate hydrates. Cement and Concrete Res. 2021;140:106268.

[30] He Y, Lu L, Struble LJ, Rapp JL, Mondal P, Hu S. Effect of calcium-silicon ratio on microstructure and nanostructure of calcium silicate hydrate synthesized by reaction of fumed silica and calcium oxide at room temperature. Mater Struct. 2014;47(1):311.

[31] Majdinasab A, Yuan Q. Synthesis of Al-substituted 11Å tobermorite using waste glass cullet: a study on the microstructure. Mater Chem Phys. 2020;250:123069.

[32] Hou D, Wu C, Yang Q, Zhang W, Lu Z, Wang P, et al. Insights on the molecular structure evolution for tricalcium silicate and slag composite: from ^{29}Si and ^{27}Al NMR to molecular dynamics. Compos Part B Eng. 2020;202:108401.

[33] Chiang Y, Chang SW. Bridging the gap between NMR measured mean silicate chain length and nano-scale silicate polymorphism of calcium silicate hydrates. Cement Concrete Res. 2021;140:106268.

[34] Li B, Li N, Brouwers H, Yu Q, Chen W. Understanding hydrogen bonding in calcium silicate hydrate combining solid-state NMR and first principle calculations. Constr Build Mater. 2020;233:117347.

[35] Maeshima T, Noma H, Sakiyama M, Mitsuda T. Natural 1.1 and 1.4 nm tobermorites from Fuka, Okayama, Japan: chemical analysis, cell dimensions, ^{29}Si NMR and thermal behavior. Cement Concrete Res. 2003;33(10):1515.

[36] Kapeluszna E, Kotwica Ł, Różycka A, Gołek Ł. Incorporation of Al in C–A–S–H gels with various Ca/Si and Al/Si ratio: microstructural and structural characteristics with DTA/TG, XRD, FTIR and TEM analysis. Constr Build Mater. 2017;155(30):643.

[37] Kong D, He G, Pan H, Weng Y, Du N, Sheng J. Influences and mechanisms of nano-C–S–H gel addition on fresh properties of the cement-based materials with sucrose as retarder. Materials. 2020;13:2345.

[38] Sáez del Bosque IF, Martínez-Ramírez S, Blanco-Varela MT. FTIR study of the effect of temperature and nanosilica on the nano structure of C–S–H gel formed by hydrating tricalcium silicate. Constr Build Mater. 2014;52:314.

[39] Ghazlan A, Ngo T, Tan P, Xie YM, Tran P, Donough M. Inspiration from nature's body armours – a review of biological and bioinspired composites. Compos Part B Eng. 2021;205(15):108513.

[40] Zhou Y, Orozco CA, Duque-Redondo E, Manzano H, Geng G, Feng P, et al. Modification of poly(ethylene glycol) on the microstructure and mechanical properties of calcium silicate hydrates. Cement Concrete Res. 2019;115:20.

[41] Meng T, Ying K, Hong Y, Xu Q. Effect of different particle sizes of nano-SiO_2 on the properties and microstructure of cement paste. Nanotechnol Rev. 2020;9(1):833.

[42] Krautwurst N, Nicoleau L, Dietzsch M, Lieberwirth I, Labbez C, Fernandez-Martinez A, et al. Two-step nucleation process of calcium silicate hydrate. Chem Mater. 2018;30(9):2895.

[43] Gebauer D, Kellermeier M, Gale JD, Bergström L, Cölfen H. Pre-nucleation clusters as solute precursors in crystallisation. Chem Soc Rev. 2014;43(7):2348.

[44] Sun Y, Peng Y, Zhou T, Liu H, Gao P. Study of the mechanical-electrical-magnetic properties and the microstructure of three-layered cement-based absorbing boards. Rev Adv Mater Sci. 2020;59:160.

[45] Zou F, Zhang M, Hu C, Wang F, Hu S. Novel C–A–S–H/PCE nanocomposites: design, characterization and the effect on cement hydration. Chem Eng J. 2021;412(15):128569.